Available online at www.sciencedirect.com
SCIENCE DIRECT®
Earth and Planetary Science Letters 244 (2006) 622–638
EPSL
www.elsevier.com/locate/epsl

Nature and evolution of Late Cretaceous lithospheric mantle beneath the eastern North China Craton: Constraints from petrology and geochemistry of peridotitic xenoliths from Jünan, Shandong Province, China

Jifeng Ying [a,*], Hongfu Zhang [a], Noriko Kita [b,1], Yuichi Morishita [b], Gen Shimoda [b]

[a] State Key Laboratory of Lithospheric Evolution, Institute of Geology and Geophysics, Chinese Academy of Sciences, P.O. Box 9825, Beijing 100029, China

[b] Geological Survey of Japan, National Institute of Advanced Industrial Science and Technology, AIST Tsukuba Central 7, Tsukuba 305-8567, Japan

Received 6 May 2005; received in revised form 10 February 2006; accepted 14 February 2006
Available online 24 March 2006
Editor: E. Boyle

Abstract

Mantle xenoliths entrained in a newly discovered Late Cretaceous basaltic breccia at Jünan, Shandong Province, China provide important constraints on the nature and evolution of the Late Mesozoic lithospheric mantle beneath the eastern North China Craton. The basaltic breccia erupted at 67 Ma contains abundant mantle and lower crustal xenoliths, including peridotites, pyroxenites, and granulites. The peridotitic xenoliths are all spinel-facies lherzolites and two types of lherzolites, high-$Mg^{\#}$ and low-$Mg^{\#}$, occur. The low-$Mg^{\#}$ lherzolites are dominant peridotitic xenoliths and have coarse-grained texture. These lherzolites are characterized by the occurrence of low $Mg^{\#}$ ($Fo<90$) olivine, orthopyroxene, and clinopyroxene and the LREE-depleted REE patterns ($(La/Yb)_N=0.3$–0.8) in cpxs. These mineral features and estimated equilibration temperatures (950–1040 °C) are very similar to those of lherzolite xenoliths entrained in the widespread Cenozoic basalts, eastern China. This similarity suggests that the low-$Mg^{\#}$ spinel lherzolites represent the newly accreted lithospheric mantle. The high-$Mg^{\#}$ lherzolites are very few and typified with high $Mg^{\#}$ olivine ($Fo=92$), high $Cr^{\#}$ spinel, and convex-upward cpx REE pattern ($(La/Yb)_N=1.5$ and $(La/Nd)_N=0.2$). Its refractory geochemical features are completely different from those of low-$Mg^{\#}$ lherzolites, but similar to those xenoliths from Archean and Proterozoic lithospheric mantle on the craton, and thus represent the relic of old refractory lithospheric mantle. The convex-upward cpx REE pattern implies an involvement of melt/rock interaction in its origin. No obvious differences in the equilibrium temperature of low- and high-$Mg^{\#}$ peridotites suggest that the newly accreted mantle was close contact with the overlying old lithospheric mantle at the time of basaltic eruption.

Keywords: basalts; peridotitic xenoliths; melt/rock interaction; lithospheric evolution; North China Craton

* Corresponding author. Tel.: +86 10 62007821; fax: +86 10 62010846.
E-mail address: jfying@mail.iggcas.ac.cn (J. Ying).
[1] Present address: Department of Geology and Geophysics, University of Wisconsin, 1215 W. Dayton Street, Madison, WI 53706-1692, USA.

0012-821X/$ - see front matter © 2006 Elsevier B.V. All rights reserved.
doi:10.1016/j.epsl.2006.02.023

1. Introduction

Co-existence of both Paleozoic kimberlites and Cenozoic basalts on the Archean North China Craton (NCC) provides a precious opportunity to investigate the temporal evolution of the sub-continental lithospheric mantle beneath the craton [1,2]. Detailed studies on mantle xenoliths, xenocrysts, and solid diamond inclusions in kimberlites at the Mengyin County (Shandong Province) and Fuxian County (Liaoning Province) show that a thick, cold and highly refractory lithospheric mantle was survived until at least mid-Ordovician [3–7], consistent with the well-accepted model that the Archean craton is underlain by thick, cold and refractory lithospheric mantle [8–11]. However, peridotitic xenoliths derived from the Neogene and Quaternary basalts from the NCC suggest a relatively hot, thin and fertile lithosphere beneath the eastern NCC in the Cenozoic [7,12]. This implies that not only lithospheric architecture such as the thickness and geotherm but also lithospheric mantle composition has considerably changed since the Phanerozoic beneath the eastern NCC. The replacement of old refractory lithospheric mantle by younger fertile one was invoked to account for the change [1,2,7,13]. However, more recent studies on Mesozoic basaltic rocks and their borne mantle xenocrysts on the craton show that other mechanisms such as lithospheric transformation through peridotite-melt interaction [14,15] and lithospheric foundering [16] could also be important in the lithospheric evolution of the region. Therefore, though the lithosphere thinning has been widely accepted, the timing and mechanism responsible for such a thinning process still remain controversial. In this paper, we report petrological and geochemical data of a suite of newly discovered mantle xenoliths entrained in a Late Cretaceous basaltic breccia at Jünan, Shandong Province using the in-situ techniques (electron microprobe and secondary ion mass spectrometer) with an aim to place further constraints on the evolution of the lithospheric mantle beneath the eastern NCC.

2. Geologic setting

The NCC, Chinese part of the Sino-Korean Craton, is one of the oldest cratons in the world with Archean crustal remnants as old as 3.8 Ga [17]. The craton is bounded by the Paleozoic–Jurassic Central Asian orogenic belt to the north and the Paleozoic–Triassic Qinling–Dabie–Sulu high–ultrahigh pressure metamorphic belt to the south and east respectively (Fig. 1). The NCC can be divided into a Western Block, an Eastern Block and a Trans-North China Orogen based on geology, geochronology, tectonic evolution and P–T–t paths of metamorphic rocks [18]. The basement of the Eastern Block is predominantly composed of Early to Late Archean tonalitic–trondhjemitic–granodioritic (TTG) gneisses and 2.5 Ga syntectonic granitoids, with Early to Late Archean granitic gneisses and supracrustal rocks. The Western Block, a stable platform, consists of Late Archean to Paleoproterozoic metasedimentary belts that unconformably overlie Archean basement. The Trans-North China Orogen, separating the Eastern and Western Blocks, is composed of Late Archean to Paleoproterozoic TTG gneisses and granitoids that are interleaved with abundant sedimentary and volcanic rocks developed in magmatic arc and intra-arc basin environments [18].

Volcanism became active in the NCC since the Paleozoic, as exemplified by the eruption of Ordovician kimberlites [3]. After a long magmatic hiatus, volcanism resumed in Late Jurassic and upsurged in Early Cretaceous and Cenozoic as shown by emplacement of voluminous Early Cretaceous volcanic rocks, alkaline and granitoid rocks [12,13,15,19–23] and extensive Tertiary to Neogene mantle and crustal xenolith-bearing basalts [24–26].

Shandong Province, situated in the central part of eastern NCC, is separated by the long-lived wrench fault—Tanlu fault zone into two parts. The western part is called Luxi and the eastern Jiaodong. The tectonics of the Jiaodong region is more complicated than that of Luxi region due to the occurrence of the Sulu ultrahigh pressure metamorphic belt that was resulted from the continental collision between the NCC and the Yangtze Craton in Late Triassic. Although this belt was traditionally regarded as the suture of the NCC and the Yangtze Craton to the east of Tanlu fault zone [27,28], more and more evidence favor a crustal-detachment model for the suturing of the NCC and the Yangtze Craton [29,30]. According to this model, the upper crust of the Yangtze Craton was detached from its lower crust and lithospheric mantle and thrust northward over the NCC for about 400 km, whereas the detached lower part of the lithospheric mantle was subducted under the NCC along a subsurface suture close to Nanjing (Fig. 1). This suggests that the lower crust and the lithospheric mantle beneath the Sulu orogenic belt should still be of a NCC feature.

3. Petrography

Jünan xenolith-bearing basaltic rocks occur as breccia dike, 20 km north of Jünan County, Shandong

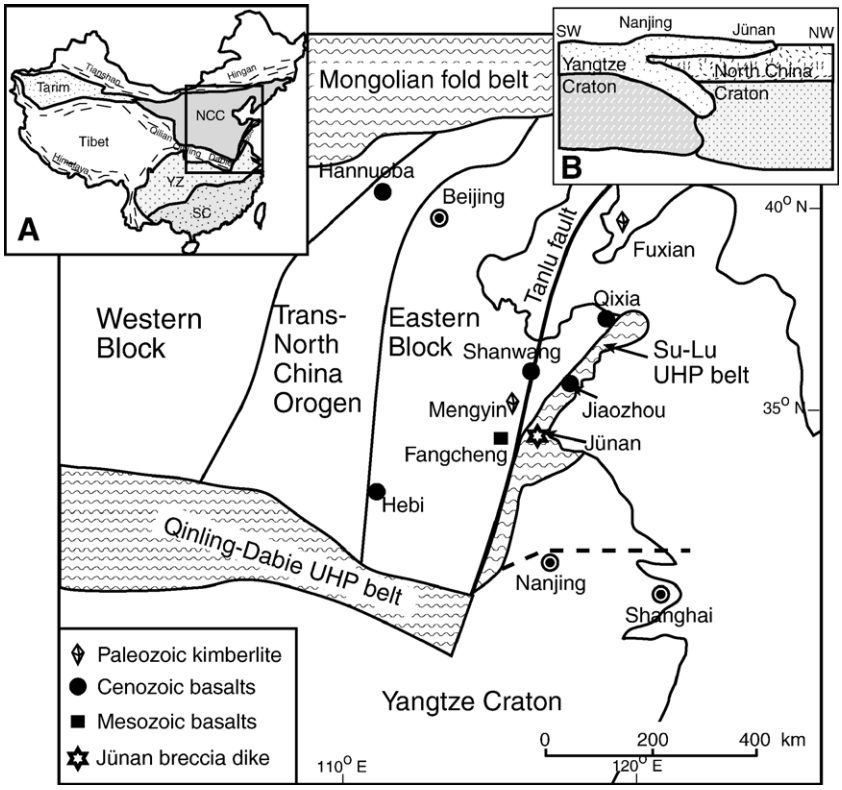

Fig. 1. Simplified geological map showing major tectonic units in eastern China and xenolith localities mentioned in the text. The dashed line refers to the sub-surface suture between the NCC and the Yangtze Craton to the east of Tanlu fault [29]. Tectonic subdivisions are based on Zhao et al. [18]. Inset (A) shows the location of the NCC relative to other cratonic blocks in China. Inset (B) illustrates the crustal detachment model for the collision of NCC with the Yangtze Craton to the east of Tanlu fault [29].

Province, which is geographically distributed in the Sulu orogenic belt. The NWW-trending dike intruded Late Mesozoic porphyritic syenite and extended up to 200 m with average width of 10 m. Whole rock K–Ar age determination on the matrix of the basaltic rocks shows that these rocks formed at Late Cretaceous (ca. 67 Ma) (Table 1).

The breccia dike exhibits a zoned structure in petrography. The margin of the dike is mainly composed of massive rocks with few (less than 10% in volume) wallrock breccias, mantle and crustal xenoliths and xenocrysts. The rock type of the breccia includes syenite, gneiss, peridotite and pyroxenite. The amount of breccias increases up to 20% from the margin to the middle part with mantle peridotites, pyroxenites and lower crustal granulites and mantle xenocrysts of mica, olivine and augite as the dominant breccias. The central part of the dike has the highest amount of breccias (up to 40% in volume) and the breccia types are same as those in the margin and middle part. Three samples of massive rocks from the margin have very similar compositions with an average MgO=11.3%, SiO_2=44.1% and (K_2O+Na_2O)=4.8%, and thus can be classified as basanite according to TAS diagram [32].

A variety of mantle and lower crustal xenoliths and megacrysts have been found in these basaltic rocks. They are dominantly spinel or spinel-free peridotites and subordinate pyroxenites (websterites and orthopyroxenites), felsic granulites and augite xenocrysts. The peridotitic xenoliths are all lherzolites, no dunite and harzburgite have been found in these basaltic rocks. In this paper, we focus on the peridotitic xenoliths only.

Table 1
K–Ar ages on whole rock powders of Jünan basaltic rocks

Sample	Rock	Weight (g)	K (%)	^{40}Ar radiogenic 10^{-10} (mol/g)	^{40}K 10^{-8} (mol/g)	Age ($\pm 2\sigma$) (Ma)
LG-7	basalt	0.01478	2.19	2.507	6.235	65.9±1.8
LG-9	basalt	0.01638	2.06	2.469	6.148	67.8±1.1

Parameters used: $\lambda_e = 0.581 \times 10^{-10}$ year^{-1}, $\lambda_\beta = 4.962 \times 10^{-10}$ year^{-1} [31].

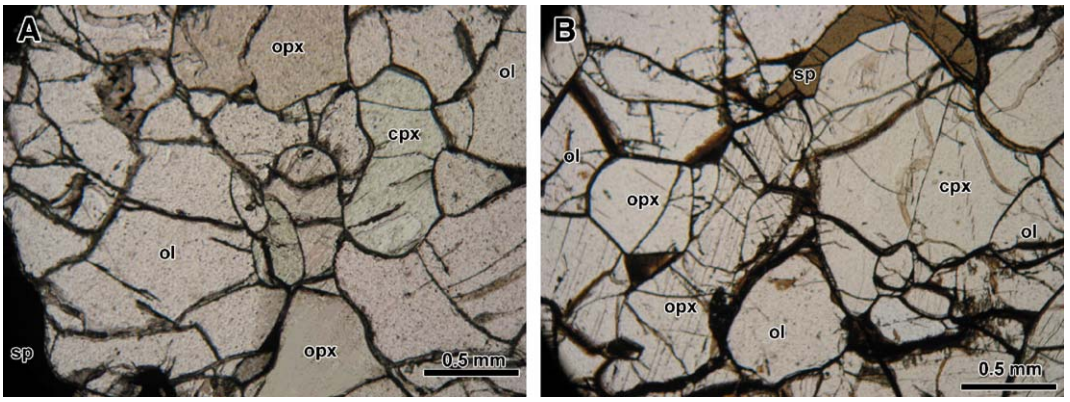

Fig. 2. Representative microphotographs of Jünan lherzolites. (A) The high-Mg# lherzolite shows granuloblastic texture (plane-polarized light). (B) The low-Mg# lherzolite has equilibrated texture with triple junctions and curved grain boundaries, exsolution lamellae can be observed in some orthopyroxene grains (plane-polarized light).

All peridotitic xenoliths are rounded with an alteration to various degrees and range from 2 to 7 cm with the majority less than 5 cm. According to the mineral compositions, two types of peridotitic xenoliths, high-Mg# and low-Mg#, occur (see next section). The high-Mg# lherzolites are coarse to medium grain sizes and have typical granuloblastic textures (Fig. 2). They generally have relatively high percentage of opx and low percentage of cpx in mineral mode, i.e. high opx/cpx ratio (Table 2). Mineral phases for these high-Mg# lherzolites are homogenous. The low-Mg# lherzolites display equilibrated texture with triple junctions and curved grain boundaries. Similarly, most of mineral phases for these low-Mg# lherzolites are homogenous except for some opx, where cpx exsolution lamellae can be occasionally observed (Fig. 2). Spinels occur as isolated phases at grain boundaries of other minerals. The mineral mode for these low-Mg# lherzolites is variable (ol = 56–78; opx = 9–24; cpx = 10–26; sp = 2–4) (Table 2), but in general, majorities of low-Mg# lherzolites have relatively high cpx and low opx contents, slightly different from the high-Mg# lherzolites. In the ol–opx–cpx classification diagram (Fig. 3), all the low-Mg# and high-Mg# peridotites are plotted in the lherzolite field and the field for the on-and off-craton peridotitic xenoliths entrained in the widespread

Table 2
Estimated modes of Jünan mantle xenoliths

Sample	Ol	Opx	Cpx	Sp
High-Mg#				
03LG-01	68	22	8	2
Low-Mg#				
03LG-03	78	17	5	
3LG-08	56	16	24	4
03LG-10	64	10	23	3
03LG-11	56	15	26	3
LG-10	57	16	23	2
03LG-12	67	9	21	3
03LG-16	60	13	23	4
04LG-9	58	24	16	3
04LG-2	71	16	11	2
04LG-8	73	14	10	3
04LG-10	67	20	10	3
04LG-11	69	11	18	2
04LG-12	62	23	12	3
04LG-01	69	16	13	2
04LG-14	59	22	17	2

Ol, olivine; Opx, orthopyroxene; Cpx, clinopyroxene; Sp, spinel.

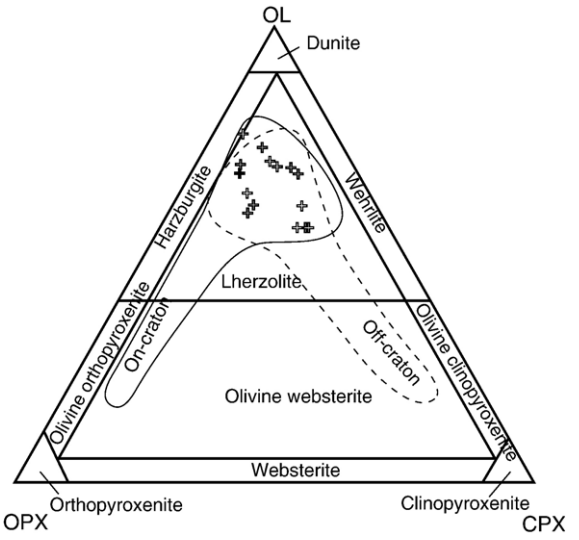

Fig. 3. Petrological classification for peridotitic xenoliths from Jünan. The open and solid crosses refer to the low-Mg# and high-Mg# peridotitic xenoliths, respectively. The on-cratonic and off-cratonic Cenozoic mantle xenoliths in eastern China are from Fan et al. [12].

Cenozoic basalts, eastern China [12]. This demonstrates that the peridotitic xenoliths in Late Cretaceous Jünan basaltic rocks have some similarities in petrology and mineralogy to those peridotitic xenoliths from the Cenozoic basalts on the craton. Water-bearing mineral phases such as phlogopite and amphibole have not been observed.

4. Analytical methods

Two whole rock samples from the margin of the dike, namely massive rocks with scarce breccias, were selected and crushed to about 60–80 mash, and then the matrix were carefully picked up under binocular microscope for K–Ar dating. The K–Ar age determination was performed at Chinese Petroleum Exploration Center using a Micromass 5400 spectrometer. Major element compositions of minerals were determined with a Cameca SX50 electron microprobe at State Key Laboratory of Lithospheric Evolution, the Institute of Geology and Geophysics, Chinese Academy of Sciences. The analyses were operated at 15 kv accelerating voltage, 10 nA current and 2 μm electron beam. Natural mineral standards were used for calibration and a PAP correction procedure was applied to the data [33].

The concentrations of Y, Sr, Zr and REE in clinopyroxene were measured in-situ with a large radius SIMS (Secondary Ion Mass Spectrometer, Cameca IMS1270) at the Geological Survey of Japan. A 25-μm diameter O^- primary ion beam was targeted on the sample surface. The primary ion intensity was between 2–5 nA. We applied both energy filtering (+40eV) and high mass resolution (mass resolving power=5000) in order to fully eliminate molecular interferences from atomic ions. The energy filtering voltage of 40 eV is somewhat lower than that of conventional REE analyses using smaller SIMS (≥100 eV by Shimizu et al. [34] and Zinner and Crozaz [35]). However, this lower offset voltage is enough to eliminate multiple matrix ion peaks and has advantage of lesser reduction of REE signals. The high mass resolution of 5000 effectively removed light REE oxide interference on the heavy REEs, which are never completely removed solely by energy filtering. A similar technique combining energy filtering and high mass resolution was already applied to the analyses of standard zircon crystals [36]. In order to completely eliminate tailing of REE-oxide mass spectrum to the REE atomic peak, a field aperture was set to be $4000\times4000\ \mu m^2$ that allows only a central $20\times20\ \mu m^2$ sample surface area to be analyzed. This ion optics is similar to the conditions that were used for trace element analyses in high mass resolution mode [37,38]. The relative sensitivity factors of trace elements (normalized to ^{30}Si) were obtained by using NIST SRM 612 as a standard [39]. Single analysis took between 1 and 4 h depending on their REE concentrations. Errors of the analyses are between a few and 30% for most analyses. In order to check the accuracy of the analyses, we also run four clinopyroxene standards, of which REE and other trace element contents were calibrated by using ICP-MS analyses, repeatedly within the same analytical sessions (see in Appendix). These results indicate that the accuracy of our analyses is within 10%.

5. Mineral compositions

Major element compositions of minerals in Jünan xenoliths are given in Table 3 and trace element concentrations of clinopyroxene are presented in Table 4. All mineral phases in these xenoliths broadly have intergranular and intra-granular homogeneity based on several core and rim analyses on minerals in each sample, and thus compositions given in Table 3 are average analyses. Two types of the peridotitic xenoliths, i.e. low-$Mg^{\#}$ and high-$Mg^{\#}$ peridotites, are presented based on the mineral compositions (Table 3).

5.1. Major elements

5.1.1. Low-$Mg^{\#}$ peridotites

Olivines from the low-$Mg^{\#}$ peridotites are characterized with low $Mg^{\#}$ (Fo<90), NiO (0.32–0.42 wt.%), CaO (<0.1 wt.%) and high MnO (>0.1 wt.%) (Table 3 and Fig. 4). Orthopyroxenes have lower $Mg^{\#}$ (<0.91), Cr_2O_3 (0.34 wt.%) and high Al_2O_3 contents than those of high-$Mg^{\#}$ peridotites. Clinopyroxenes have low $Mg^{\#}$ (<0.91), high Al_2O_3 (5.7–7.3 wt.%), Cr_2O_3 (0.53–1.14 wt.%) and Na_2O (1.3–1.9 wt.%) and can be named as Cr-diopsides. Accordingly, the low-$Mg^{\#}$ peridotites belong to the Cr-diopside suite of Wilshire and Shervais [40] or type I of Frey and Prinz [41]. Spinels are characterized with low $Cr^{\#}$ (0.03–0.17). These mineral features and mineral assemblage are very similar to those for the Cenozoic lherzolites in eastern China and spinel-facies low-$Mg^{\#}$ peridotites from the Cenozoic basalts, Hebi locality, China [7] (Fig. 4).

5.1.2. High-$Mg^{\#}$ peridotites

Olivines from a high-$Mg^{\#}$ peridotite are distinctive from the low-$Mg^{\#}$ peridotites in that they have much higher $Mg^{\#}$ (Fo=92), NiO (0.38 wt.%) and lower MnO (0.11 wt.%) (Table 3 and Fig. 4), which fall within the field for olivines from the mantle peridotitic xenoliths

Table 3
Representive electron microprobe analyses of minerals from Jünan mantle xenoliths

Sample	03LG-01				03LG-03			03LG-08				03LG-10			
Rock	spinel lherzolite				lherzolite			spinel lherzolite				spinel lherzolite			
Mineral	Ol	Cpx	Opx	Sp	Ol	Cpx	Opx	Ol	Cpx	Opx	Sp	Ol	Cpx	Opx	Sp
Point	9	6	6	3	4	2	2	7	6	2	2	4	1	2	2
SiO_2	40.9	53.2	56.4	0.08	40.5	52.2	55.8	40.4	51.1	54.1	0.03	40.0	50.9	54.5	0.12
TiO_2	0.05	0.19	0.08	0.32	0.02	0.72	0.08	0.03	0.66	0.15	0.18	0.02	0.64	0.11	0.16
Al_2O_3	0.02	3.26	2.65	26.2	0.03	7.61	4.92	0.02	7.54	5.39	60.3	0.01	7.30	5.05	57.3
Cr_2O_3	0.05	1.35	0.74	41.5	0.00	0.77	0.36	0.03	0.53	0.27	7.00	0.00	0.86	0.39	9.75
FeO	8.27	2.64	5.19	14.4	10.31	3.10	6.73	11.1	3.42	7.02	11.8	10.0	3.28	6.55	11.6
MnO	0.11	0.08	0.10	0.14	0.15	0.11	0.16	0.16	0.08	0.12	0.11	0.16	0.15	0.14	0.06
MgO	49.8	17.7	33.4	16.6	48.1	14.9	32.5	48.6	15.4	32.4	21.0	49.6	15.4	32.9	20.7
CaO	0.10	20.9	1.15	0.01	0.07	19.72	0.67	0.06	19.5	0.81	0.00	0.08	19.6	0.81	0.01
Na_2O	0.01	0.73	0.06	0.01	0.03	1.89	0.12	0.01	1.75	0.12	0.01	0.01	1.80	0.12	0.01
NiO	0.38	0.08	0.09	0.21	0.34	0.12	0.12	0.36	0.03	0.06	0.40	0.37	0.06	0.07	0.38
Total	99.7	100.1	99.8	99.5	99.5	101.2	101.4	100.8	100.1	100.5	100.9	100.3	100.1	100.6	100.1
$Mg^{\#}$	0.92	0.92	0.92	0.67	0.89	0.90	0.89	0.88	0.89	0.89	0.76	0.90	0.89	0.89	0.76
$Cr^{\#}$				0.52							0.07				0.10

Sample	03LG-11				LG-10				03LG-12				03LG-16			
Rock	spinel lherzolite				spinel lherzolite				spinel lherzolite				Spinel lherzolite			
Mineral	Ol	Cpx	Opx	Sp	Ol	Cpx	Opx	Sp	Ol	Cpx	Opx	Sp	Ol	Cpx	Opx	Sp
Point	8	13	3	3	4	7	5	2	5	5	2	2	4	5	4	5
SiO_2	40.3	51.3	54.1	0.06	40.8	50.3	53.4	0.00	40.3	51.3	54.5	0.05	40.7	52.2	55.59	0.05
TiO_2	0.03	0.56	0.14	0.15	0.02	0.69	0.20	0.02	0.02	0.65	0.15	0.19	0.05	0.60	0.17	0.16
Al_2O_3	0.02	7.28	5.13	58.2	0.01	8.28	5.94	63.5	0.01	7.47	5.18	59.0	0.02	7.22	5.04	57.7
Cr_2O_3	0.03	0.74	0.34	9.21	0.02	0.27	0.16	2.73	0.01	0.73	0.35	8.32	0.04	0.68	0.35	8.51
FeO	10.9	3.22	6.83	11.2	10.7	4.15	8.13	13.6	10.8	3.71	6.85	11.0	10.6	3.16	6.77	10.9
MnO	0.17	0.11	0.14	0.08	0.13	0.17	0.20	0.00	0.15	0.11	0.15	0.12	0.14	0.08	0.12	0.10
MgO	48.7	15.5	32.5	20.6	48.2	14.6	30.7	20.2	49.0	15.4	32.7	20.9	48.3	15.1	32.1	20.8
CaO	0.09	19.4	0.83	0.00	0.05	19.6	0.79	0.00	0.08	19.4	0.84	0.01	0.07	19.1	0.81	0.00
Na_2O	0.02	1.78	0.14	0.01	0.02	1.65	0.14	0.01	0.02	1.85	0.13	0.00	0.03	1.88	0.15	0.01
NiO	0.32	0.07	0.12	0.35	0.42	0.02	0.06	0.28	0.36	0.05	0.10	0.36	0.34	0.04	0.15	0.35
Total	100.6	100.0	100.3	99.9	100.4	99.6	99.7	99.9	100.8	100.1	101.0	99.9	100.3	100.2	101.3	98.7
$Mg^{\#}$	0.89	0.90	0.89	0.76	0.89	0.86	0.86	0.73	0.89	0.90	0.89	0.76	0.89	0.89	0.89	0.77
$Cr^{\#}$				0.10				0.03				0.09				0.09

(continued on next page)

Table 3 (*continued*)

Sample	04LG-9				04LG-2				04LG-8				04LG-10			
Rock	Spinel lherzolite				Spinel lherzolite				Spinel lherzolite				Spinel lherzolite			
Mineral	Ol	Cpx	Opx	Sp	Ol	Cpx	Opx	Sp	Ol	Cpx	Opx	Sp	Ol	Cpx	Opx	Sp
Point	3	3	3	3		4	4		4	5	4	3	4	5	4	3
SiO_2	41.3	51.9	54.9	0.10	41.2	53.2	55.4	0.04	40.9	52.6	55.8	0.07	41.2	51.8	55.5	0.08
TiO_2	0.01	0.63	0.19	0.18	0.00	0.37	0.09	0.12	0.06	0.66	0.15	0.16	0.00	0.72	0.11	0.17
Al_2O_3	0.05	7.35	5.21	57.7	0.00	5.68	3.86	51.4	0.01	7.12	4.88	56.6	0.02	7.31	4.80	58.5
Cr_2O_3	0.03	0.71	0.41	9.04	0.03	1.14	0.25	15.5	0.01	0.78	0.39	10.3	0.00	0.71	0.35	8.09
FeO	10.53	3.22	6.51	10.9	10.6	2.98	6.78	12.7	10.5	3.07	6.72	11.2	10.7	3.11	6.87	11.4
MnO	0.16	0.07	0.14	0.08	0.14	0.07	0.17	0.05	0.17	0.10	0.14	0.07	0.14	0.12	0.16	0.11
MgO	48.9	15.5	32.4	20.9	48.5	15.4	33.0	19.1	49.0	15.1	32.5	20.6	48.8	14.9	32.5	21.0
CaO	0.07	19.1	0.93	0.01	0.01	20.9	0.66	0.00	0.05	19.7	0.74	0.00	0.04	19.6	0.71	0.00
Na_2O	0.01	1.90	0.19	0.01	0.01	1.30	0.04	0.01	0.02	1.94	0.13	0.00	0.01	1.98	0.09	0.00
NiO	0.32	0.06	0.11	0.42	0.36	0.06	0.07	0.36	0.36	0.06	0.10	0.34	0.36	0.01	0.09	0.39
Total	101.3	100.4	101.0	99.4	100.8	101.3	101.5	99.2	101.1	101.1	101.5	99.3	101.4	100.4	101.2	99.8
$Mg^{\#}$	0.89	0.90	0.91	0.77	0.89	0.90	0.90	0.73	0.89	0.90	0.90	0.77	0.89	0.90	0.90	0.77
$Cr^{\#}$				0.10				0.17				0.11				0.08

Sample	04LG-11				04LG-12				04LG-01				04LG-14		
Rock	Spinel lherzolite				Spinel lherzolite				Spinel lherzolite				lherzolite		
Mineral	Ol	Cpx	Opx	Sp	Ol	Cpx	Opx	Sp	Ol	Cpx	Opx	Sp	Ol	Cpx	Opx
Point	4	3	3	3	4	4	3	3	3	3	3	3	3	3	3
SiO_2	41.1	52.8	56.1	0.03	41.2	52.2	54.5	0.11	40.8	51.8	54.5	0.08	40.9	52.4	54.9
TiO_2	0.03	0.50	0.14	0.18	0.03	0.60	0.06	0.11	0.00	0.69	0.20	0.20	0.02	0.64	0.16
Al_2O_3	0.01	6.14	4.22	52.8	0.02	7.05	4.93	56.5	0.05	7.47	5.20	57.4	0.02	7.19	5.08
Cr_2O_3	0.02	0.93	0.43	14.1	0.02	0.75	0.38	10.1	0.03	0.73	0.33	8.33	0.03	0.76	0.39
FeO	9.71	2.70	6.23	11.3	10.1	3.01	6.46	10.9	10.2	3.07	6.39	10.4	10.5	3.14	6.65
MnO	0.13	0.07	0.12	0.12	0.12	0.08	0.21	0.08	0.14	0.08	0.15	0.11	0.19	0.12	0.14
MgO	49.5	15.4	33.2	20.2	49.0	15.6	32.5	21.1	48.8	15.1	32.3	21.2	48.7	15.4	32.4
CaO	0.06	20.6	0.69	0.00	0.09	19.1	0.94	0.01	0.09	18.6	0.89	0.01	0.02	19.1	0.84
Na_2O	0.02	1.66	0.10	0.02	0.03	1.73	0.17	0.01	0.03	1.85	0.17	0.01	0.01	1.85	0.21
NiO	0.41	0.09	0.10	0.33	0.38	0.09	0.12	0.33	0.37	0.07	0.09	0.35	0.33	0.03	0.08
Total	100.9	100.9	101.4	99.1	100.9	100.2	100.2	99.3	100.4	99.5	100.2	98.1	100.7	100.6	100.9
$Mg^{\#}$	0.90	0.91	0.90	0.76	0.89	0.90	0.90	0.77	0.89	0.90	0.91	0.78	0.89	0.89	0.91
$Cr^{\#}$				0.15				0.11				0.09			

Table 4
Trace element abundances (ppm) in clinopyroxenes from Jünan mantle xenoliths

	High-Mg#	Low-Mg#					
Sample	03LG-01	03LG-03	03LG-08	03LG-10	03LG-11	03LG-12	LG-10
Points	8	3	4	3	4	3	2
La	1.3	0.9	1.4	0.8	2.5	1.0	2.1
Ce	6.6	3.7	5.2	3.3	6.1	3.4	7.2
Pr	1.8	0.8	0.9	0.7	0.9	0.6	1.3
Nd	13	4.6	5.4	4.0	4.6	4.0	7.9
Sm	3.9	1.9	1.9	1.6	1.7	1.7	2.8
Eu	1.2	0.7	0.8	0.7	0.7	0.7	1.0
Gd	3.3	2.6	2.8	2.4	2.6	2.6	3.5
Tb	0.4	0.4	0.5	0.5	0.5	0.5	0.6
Dy	2.3	3.3	4.1	3.2	3.3	3.5	4.3
Ho	0.4	0.7	0.9	0.7	0.7	0.8	1.0
Er	1.1	2.1	2.8	2.0	2.2	2.2	2.7
Tm	0.1	0.3	0.4	0.3	0.3	0.3	0.4
Yb	0.6	1.9	2.8	1.9	2.2	2.3	2.4
Lu	0.1	0.3	0.4	0.3	0.3	0.3	0.4
Sr	194	74	81	71	86	75	80
Y	9.9	19	25	20	20	21	26
Zr	24	36	34	32	33	33	31
ΣREE	36	24	30	22	29	24	38
$(La/Yb)_N$	1.5	0.3	0.3	0.3	0.8	0.3	0.6

and xenocrysts entrained in Paleozoic kimberlites on the craton and also close to the field for the olivines from high-Mg# peridotitic xenoliths in Hebi Cenozoic basalts (Fig. 4). Orthopyroxenes from high-Mg# peridotites have higher Mg# (0.92), Cr_2O_3 (0.74 wt.%) and lower Al_2O_3 (2.65 wt.%) than corresponding values of opxs from the low-Mg# peridotites. Clinopyroxenes in the high-Mg# peridotites also have highest Mg# (0.92), Cr_2O_3 (1.35 wt.%) and lowest Al_2O_3 (3.26 wt.%), TiO_2 (0.19 wt.%) and Na_2O (0.73 wt.%) relative to the low-Mg# peridotites (Table 3 and Fig. 4), falling within the field for the high-Mg# peridotites from Hebi Cenozoic basalts. Spinel has much higher Cr_2O_3 ($Cr^{\#}=0.52$) than those from the low-Mg# peridotites (Table 3 and Fig. 4). In summary, compositional features of all constituent minerals from the high-Mg# peridotites are completely different from those of low-Mg# peridotites, but similar to those from peridotitic xenoliths and xenocrysts sampled by the Paleozoic kimberlites and the high-Mg# peridotites in Hebi Cenozoic basalts [7].

5.2. Trace elements of clinopyroxenes

5.2.1. Low-Mg# peridotites

Clinopyroxenes of the low-Mg# peridotites have low REE contents (∑REE=22—38 ppm) (Table 4) and majorities show slightly LREE depleted chondrite-normalized patterns ($(La/Yb)_N=0.3$—0.8) (Fig. 5). The LREE-enriched profiles which are commonly observed in clinopyroxenes from Cenozoic peridotitic xenoliths in eastern China have not been observed in the Jünan xenoliths [12]. One sample (03LG-11) displays a slightly LREE-enriched (La and Ce), i.e. spoon-shaped REE pattern (Fig. 5). This implies that few xenoliths would have been affected by the chromatographical metasomatism [44]. High field strength elements (HFSE) such as Zr and Ti in these cpxs exhibit slight negative anomalies (Fig. 5).

5.2.2. High-Mg# peridotites

Clinopyroxene of high-Mg# peridotite has a distinctive trace element feature. It has much lower HREE concentration than those of the cpxs from low-Mg# peridotites in spite of relatively high REE abundance (∑REE=36 ppm) and show a convex-upward chondrite-normalized REE pattern with the maximum at Nd and very steep slope from Nd to Lu ($(La/Yb)_N=1.5$ and $(La/Nd)_N=0.2$) (Table 4 and Fig. 5). Clinopyroxene from high-Mg# peridotite also shows a HFSE depletion, especially for Ti and Zr (Fig. 5). Sr enrichment relative to the neighboring LREE is also apparent.

6. Temperature estimation

As stated in previous sections, the mineral phases in these peridotitic xenoliths posses equilibrated textures and have achieved chemical homogeneity, thus these mineral assemblages can be used for equilibration temperature estimation. Equilibration temperatures of the Jünan peridotitic xenoliths estimated with different thermometers are given in Table 5 and plotted in Fig. 6. These results are reliable as there is a roughly positive correlation between temperatures calculated with different thermometers. Although the thermometer of *T* (BK) based on Ca-in-opx is sensitive to small differences in calibration and would cause considerable scatter while plotted against two-pyroxene thermometers [51], the Jünan peridotitic xenoliths do not show such a feature in that temperatures estimated through different thermometers correlate well except for sample 04LG-2. The estimated temperatures of the low-Mg# peridotites fall within the range of 950–1040 °C (Table 5), and the total range of temperatures in low-Mg# peridotites is higher than that of Qixia but similar to that of Shanwang, both of which are Cenozoic peridotitic xenolith-bearing basaltic field and distributed in Shandong Province [42] (Fig. 1). The high-Mg# peridotite yields a comparable or slightly higher

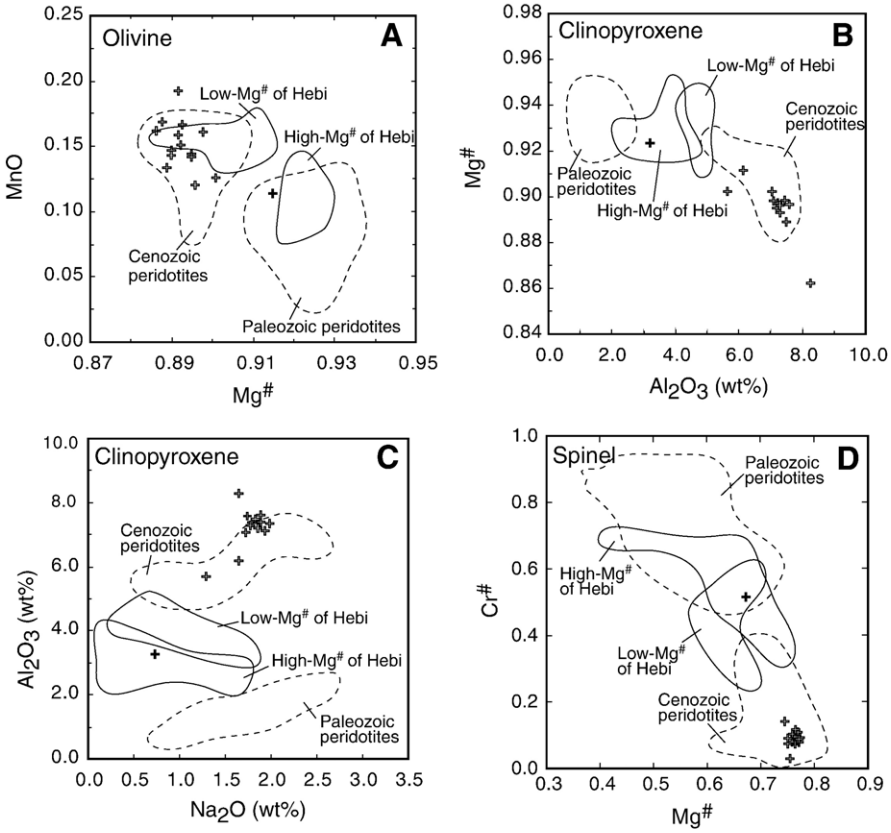

Fig. 4. (A) $Mg^{\#}$ vs. MnO of olivines from mantle xenoliths in Jünan. (B) Al_2O_3 vs. $Mg^{\#}$ of clinopyroxene from mantle xenoliths in Jünan. (C) Al_2O_3 vs. Na_2O of clinopyroxene from mantle xenoliths in Jünan. (D) $Cr^{\#}$ vs. $Mg^{\#}$ of spinels from mantle xenoliths of Jünan. Symbols as same in Fig. 3. Paleozoic, Cenozoic and Hebi data are from Zheng et al. [7,42,43].

temperature than those of low-$Mg^{\#}$ peridotites except that the thermometer of *T* (BK) gave a much higher temperature.

It is difficult to estimate equilibrium pressure for these xenoliths due to a lack of reliable geobarometer, however, their equilibrium temperature may be used to reflect the depth with an assumption that xenoliths were equilibrated under the same geotherm. There is no significant difference between the equilibrium temperatures of the low-$Mg^{\#}$ and high-$Mg^{\#}$ peridotites, implying that they might reside in a similar depth prior to be entrapped in the host basaltic magmas.

7. Discussion

7.1. Origin of Jünan peridotitic xenoliths

7.1.1. Partial melting and metasomatism

It has been demonstrated that incompatible trace elements in anhydrous spinel peridotites preferentially partition into clinopyroxene, whilst some HFSE (Zr and Ti) and HREE (Dy, Er and Yb) have moderately high partition coefficients in orthopyroxene [52], and their partition coefficients between clinopyroxene and orthopyroxene are always greater than one unity [52,53]. Thus, clinopyroxene in anhydrous mantle peridotites is the main repository of incompatible trace elements and its trace element composition can be used to interpret the mantle processes such as partial melting, metasomatism and sub-solidus re-equilibration.

The major and trace elemental features of the constituent minerals in the Jünan peridotitic xenoliths reflect two stages of mantle processes involved in their origin: partial melting and metasomatic processes within the upper mantle. Slightly LREE-depleted REE patterns observed in almost all the clinopyroxenes from the low-$Mg^{\#}$ peridotitic xenoliths indicate that these peridotites were originated from very low degree of partial melting. The major element characteristics and relations with the trace elements in these peridotitic xenoliths, such as the depletion of HREE, Y, Al and Na of clinopyroxenes with the increases in $Mg^{\#}$, the decrease in MnO of

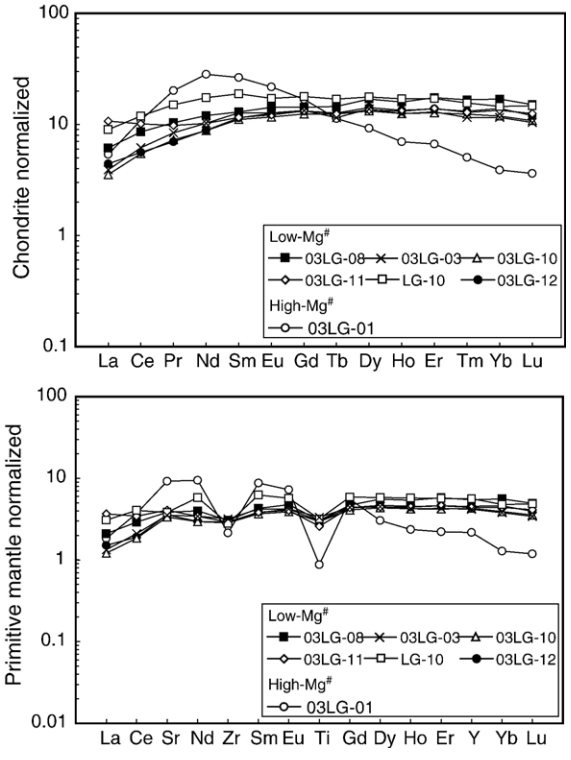

Fig. 5. (a) Chondrite-normalized REE patterns of clinopyroxenes from Jünan mantle xenoliths. The high-Mg# peridotite has the lowest HREE concentration, suggesting a higher degree of partial melting than the low-Mg# peridotites. Chondrite values are from Anders and Grevesse [45]. (b) Primitive mantle normalized trace element patterns of clinopyroxenes in Jünan mantle xenoliths. Normalization data are from Sun and McDonough [46].

olivines with the increases in Mg# and associated higher Cr#, are all consistent with a melt extraction process from the mantle. The Cr# of spinel and coexisting clinopyroxene is a sensitive indicator for the extent to which mantle peridotites have lost their basaltic components [41,54], thus the low Cr# values of spinels from the low-Mg# peridotites also indicate that these xenoliths were subjected to low degree of melt extraction. The spoon-shaped REE patterns in cpxs from some low-Mg# peridotites imply that some low-Mg# peridotites were affected by chromatographic metasomatism during which the enrichment front of the highly incompatible elements migrated faster than that of less compatible elements [55].

For the high-Mg# peridotite, the highly refractory major element compositions of constituent minerals such as high Mg# in olivine, high Cr# in spinel and much lower HREE concentration in cpx, suggest high degree of partial melting. However, the mineral composition deviated from the partial melting trend implies that the high-Mg# peridotite is not simple residue of partial melting, for instance, both the enrichment of Na_2O in cpx and higher TiO_2 in spinel require reaction with melt after high degree of melting (Fig. 7). The convex-upward REE pattern and the enrichment in incompatible elements such as Nd and Sr, as well as the depletion in HFSE (Fig. 5), are also consistent with the melt process or mantle metasomatism involved in their origin after the high degree of partial melting. Especially the convex-upward REE pattern is diagnostic of equilibrium with LREE-rich melts [55,57]. The above mentioned features in the high-Mg# peridotite are very similar to the "reactive" harzburgites from Huinan, NE China, which were regarded as products of melt-rock reaction [56]. The melts in equilibrium with the high-Mg# peridotite should be high in LREE and LILE and low in HFSE, somewhat similar to the features of Mesozoic calc-alkali volcanic rocks and carbonatites in Shandong Province [15,19,58,59].

7.1.2. Modeling calculation

The degree of partial melting (batch or fractional melting) can be constrained by modeling calculation on the basis of incompatible element concentrations of clinopyroxenes [60,61]. In this paper, we adopted the batch melting and fractional melting curves of Norman [61] with an assumption that the clinopyroxene was the

Table 5
Temperature (°C) estimations for Jünan mantle xenoliths

Sample	*T* (Wells)	*T* (SS)	*T* (WS, 1)	*T* (WS, 2)	*T* (BK)
High-Mg#					
03LG-01	1067	1079	1040	1094	1094
Low-Mg#					
03LG-03	987		989		960
03LG-08	1002	1075	967	992	1002
03LG-10	995	1061	1010	1004	1002
03LG-11	1007	1059	986	996	1010
LG-10	986	1140	964	1021	1002
03LG-12	1002	1057	1001	986	1010
03LG-16	1019	1043	979	974	1002
04LG-9	1023	1061	1017	998	1033
04LG-2	1071	969	900	949	951
04LG-8	981	1037	986	982	977
04LG-10	961	1024	970	950	969
04LG-11	956	991	987	963	960
04LG-12	1029	1043	991	988	1040
04LG-01	1033	1057	989	989	1025
04LG-14	1018		1010		1010

T (Wells): cpx–opx thermometer of Wells [47]; *T* (SS): spinel–opx thermometer of Sachtleben and Seck [48]; *T* (WS, 1) and *T* (WS, 2) are Cr–Al–opx thermometer and spinel–opx Thermometer of Witt-Eickschen and Seck [49]; T(BK): Ca-in-opx thermometer of Brey and Kohler [50] assuming pressure of 1.5 GPa.

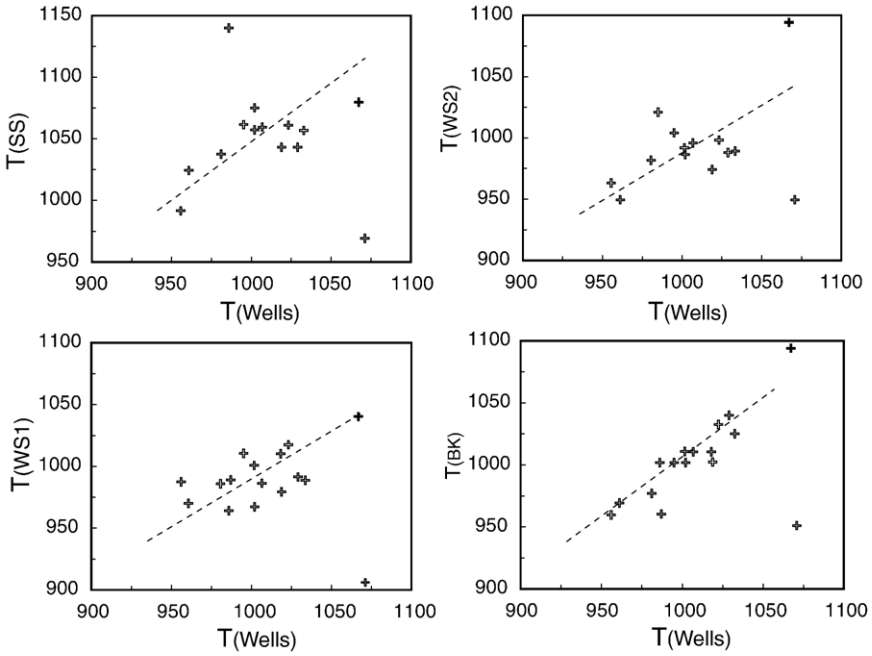

Fig. 6. Comparison of equilibration temperatures estimated with different thermometers. See Table 5 for abbreviations. Symbols as same in Fig. 3.

only phase contribution to the bulk partition coefficient in the residual assemblage (Fig. 8). The Y vs. Yb plot shows that all the low-Mg# peridotites have HREE concentrations consistent with <3% partial melting, irrespective of batch or fractional melting, since in low degree of melting the Y and HREE concentrations are insensitive to melting style. For the high-Mg# peridotite, it follows both batch and fractional melting trend with little deviation, the degree required for batch melting is about 25% and for fractional melting of 12%. However, simple estimation according to spinel Cr# yields 17% fractional melting for the high-Mg# peridotite [54]. This means that some HREE might be introduced into the peridotites during the melt/rock reaction process.

As shown in Fig. 5, Zr and Sr concentrations can be modeled by partial melting process for the low-Mg# peridotites. However, for the high-Mg# peridotitic xenolith, it shifts to the right of the melting curves. This suggests that a later addition of these elements existed in the high-Mg# peridotitic xenolith, consistent with the melt-rock reaction required from the REE and major elements of the high-Mg# peridotite.

In summary, the low-Mg# peridotites have relatively simple history and majorities were formed by the low degree (<3%) of partial melting with little affection of melt percolation process. However, the high-Mg# peridotite records a complicated history, it experienced at least a large degree of partial melting that formed the highly refractory protolith, a melt-rock reaction that led to a slight increase in opx/cpx ratio, a lowering of Mg# in olivines [56,62], an enrichment in incompatible elements, and a depletion in HFSEs.

7.2. Newly accreted lithospheric mantle

It is widely accepted that the major elements of mantle xenoliths such as olivine Mg# and olivine mode are very useful in distinguishing Archean and Phanerozoic mantle xenoliths [63], though there are opinions that osmium-based age determination is more reliable to discriminate the Proterozoic and Phanerozoic mantle [51,64]. In this paper, Os analytical work was hampered due to the small sizes of the xenoliths. Systematical and comparative studies of the petrology, mineralogy and Sr–Nd isotopic geochemistry on the spinel lherzolite xenoliths entrained in the Cenozoic basalts, eastern China, demonstrate that those lherzolite xenoliths represent newly accreted lithospheric mantle formed by low degree of partial melting [12]. The low-Mg# spinel lherzolites in Late Cretaceous Jünan breccia have the petrology, i.e. mineral assemblage (Fig. 3) and major elemental compositions (Fig. 4) that completely fall within the field for the Cenozoic peridotitic xenoliths. In the plot of olivine mode vs. olivine Mg#, these lherzolites also fall within the field for the Phanerozoic lherzolite xenoliths [11] and have an “oceanic” trend [63]. These similarities in petrological and mineralogical features suggest the low-Mg# lherzolite xenoliths

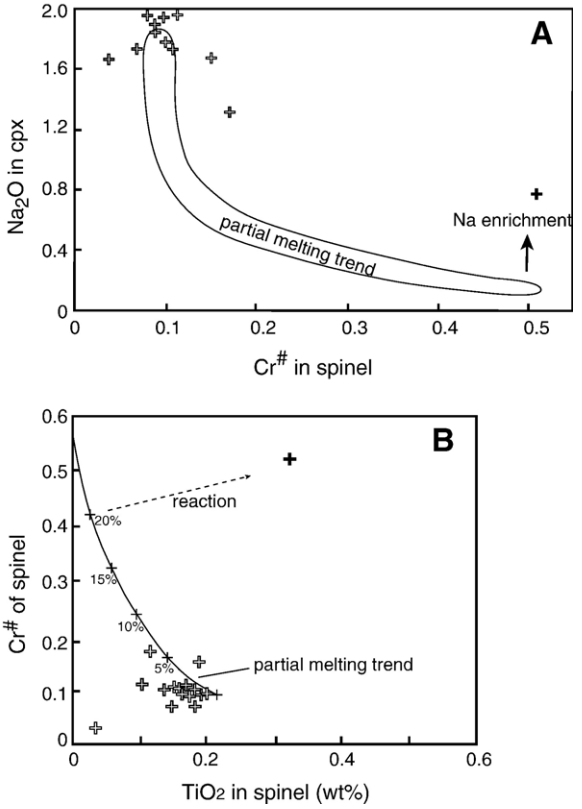

Fig. 7. $Cr^{\#}$ in spinel vs. Na_2O in clinopyroxene (A) and TiO_2 in spinel (B) of Jünan xenoliths. The higher Na_2O and TiO_2 in cpx and spinel from high-$Mg^{\#}$ peridotite imply melt/rock interaction after high degree of partial melting. Partial melting trend and parameters used are as same as the reference in [56].

were produced in a similar manner as those lherzolite xenoliths in Cenozoic basalts. This conclusion is also supported by the trace element features of clinopyroxenes such as slightly LREE-depleted patterns (Fig. 5). Thus, these spinel lherzolites represent the newly accreted lithospheric mantle. This implies that the newly accreted lithospheric mantle was widespread in the region in the Late Cretaceous, which occurred much earlier than the previous estimation as indicated by the xenoliths entrained in Neogene and Quaternary basalts [51].

7.3. Remnant of old refractory lithospheric mantle

The most significant feature for the old lithospheric mantle (Archean or Proterozoic), which distinguishes from their Phanerozoic counterpart, is the presence of highly refractory harzburgites with less abundance of lherzolites [11,63]. Most of the Archean refractory lherzolites contain low modal proportions of clinopyroxene and in general, the lherzolites become progressively less refractory from Archean through Proterozoic to Phanerozoic lithospheric mantle [11]. The Archean sub-continental refractory lithospheric mantle is commonly interpreted as the residue of high degree partial melting of primitive mantle with pyrolite composition at depth [63,65], though melt/rock reaction and cumulate processes were proposed to explain some features such as high proportion of orthopyroxenes in mantle peridotitic xenoliths from Kaapvaal Craton [66–68].

Previous studies on the mantle peridotitic xenoliths and xenocrysts from the Paleozoic kimberlites demonstrate that the dominant rock types of the lithospheric mantle beneath the NCC were refractory garnet-and spinel-facies harzburgites and cpx-poor lherzolites [2,3,69], similar to those of Kaapvaal Craton. As shown in Fig. 4, the mineral compositions (olivine and clinopyroxene) of the Jünan high-$Mg^{\#}$ xenolith fall in or close to the field for refractory peridotites from the Paleozoic kimberlites in terms of high $Mg^{\#}$, low MnO, Al_2O_3 and Na_2O contents. Occurrence of high Cr spinel rather than low Cr species in the high-$Mg^{\#}$ xenolith also show chemical similarity to the chromites from peridotitic xenoliths in Mengyin and Fuxian kimberlites. In the correlation diagram of olivine mode vs. $Mg^{\#}$, the high-$Mg^{\#}$ xenolith falls in the field for Archean/Proterozoic lherzolites and harzburgites from worldwide localities (Fig. 9). All these features suggest that the high-$Mg^{\#}$ peridotite represents a remnant of the old refractory lithospheric mantle though it is difficult to tell precisely whether it is Archean or Proterozoic. This indicates that the old and refractory lithospheric mantle would still remain in the region in the Late Cretaceous time.

7.4. Modification and reconstruction of lithospheric mantle

The high opx/cpx ratios and the enrichment of Na_2O in cpx and TiO_2 in spinel imply that the high-$Mg^{\#}$ peridotite underwent melt–rock interaction [56]. The convex-upward cpx REE patterns are usually referred to cumulative origin such as megacrysts in basalts or derivation from cpx-poor lherzolites or harzburgites which have undergone melt–rock interaction. Obviously, the refractory features of the high-$Mg^{\#}$ peridotite are different from those of magmatic segregates which should be rich in Al_2O_3 and CaO, thus the cumulative origin of the high-$Mg^{\#}$ peridotite can be ruled out. Melt percolation and reaction were applied to interpret the convex-upward REE patterns of Huinan harzburgite xenoliths from NE China and poikiloblastic harzburgite

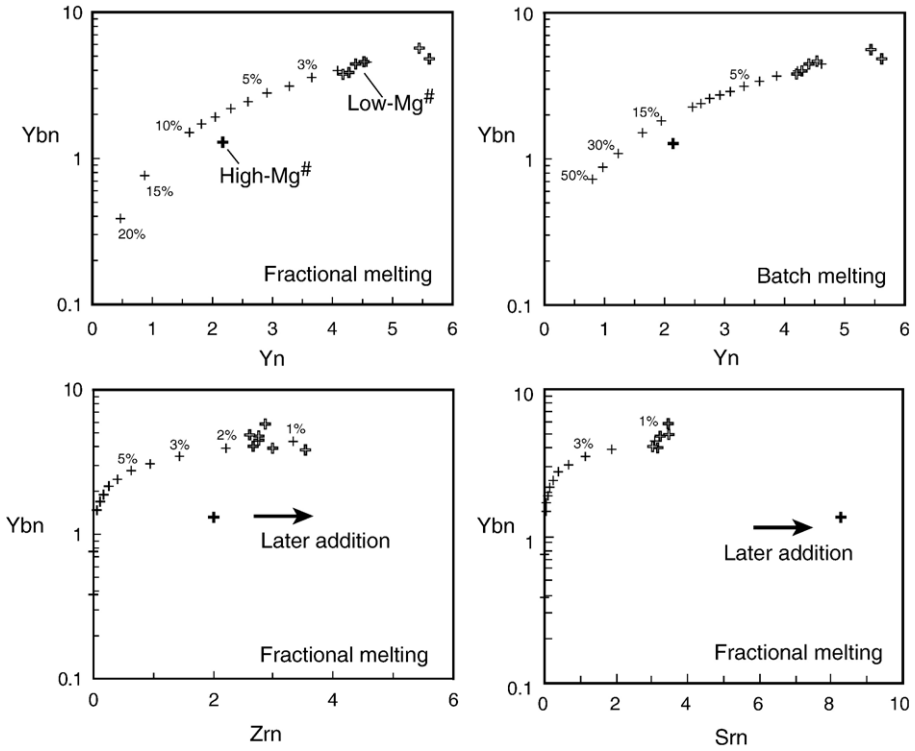

Fig. 8. Diagrams for partial melting modeling with an assumption of a primitive mantle source using trace elements in clinopyroxenes for Jünan peridotitic xenoliths. The subscript n denotes the primitive mantle normalized element concentrations. The later addition of Sr and Zr after melting is required. The low-Mg# lherzolites can be modeled by less than 3% of either fractional or batch melting and do not appear to have been affected by late stage metasomatism. Primitive mantle abundances are from Sun and McDonough [46]. Distribution coefficients (D_{cpx}), Y 0.42, Yb 0.40, Sr 0.1, Zr 0.12, and equations of Norman [61] are used for this modeling. Symbols as same in Fig. 3.

xenoliths from France [56,62]. During the melt–rock reaction, melt dissolved cpx with introduction of LREE and LILE and formed cpx-poor lherzolite or harzburgites [14,66], petrological evidence for such a process was recorded in the polymict peridotitic xenoliths from South Africa [70]. Recent studies on zoned olivine xenocrysts in Early Cretaceous Fangcheng basalts, southern part of NCC revealed that peridotite–melt reaction may convert the high-Mg# peridotite to the low-Mg# peridotites [14], which could be the reason why the high-Mg# peridotite from Jünan plot in the lower part of the field for Archean lherzolites and harzburgite (Fig. 9). In other words, the olivines from the protolith of the high-Mg# peridotite may have much higher Mg# values than what we observed now.

Though the dramatic change of the lithospheric architecture during the Phanerozoic time in eastern part of the NCC was recognized a decade ago, the timing and mechanism responsible for such a change remain unsolved. It is generally believed that the lithosphere thinning or removal accomplished in the Late Cenozoic through comparative studies of the xenoliths from Paleozoic kimberlites and Neogene and Quaternary basalts [1,13,51]. Based on the transition of basaltic source from lithospheric mantle to asthenosphere, Xu [13] proposed that the Late Cretaceous marked the end of lithospheric thinning. However, Zhang et al. [58] and Yang et al. [22] suggested that the lithospheric removal occurred in the Early Cretaceous according to widespread volcanic rocks and granites at that time. The lithospheric thinning and change perhaps commenced much earlier, possibly in the Early Jurassic as signed by occurrence of alkaline magmatism in the region [21]. In the Jünan case, the predominant low-Mg# lherzolite xenoliths and scarce high-Mg# lherzolite xenolith indicate that the old refractory lithospheric mantle beneath the Jünan region had been considerably removed and occupied by newly accreted lithospheric mantle as inferred from the low-Mg# peridotites. Thus, the dramatic lithospheric thinning must have accomplished and the accretion of lithospheric mantle has commenced before the eruption of Jünan basaltic breccia, i.e. the Late Cretaceous. Yan et al. [71] came to a similar conclusion based on the investigation of

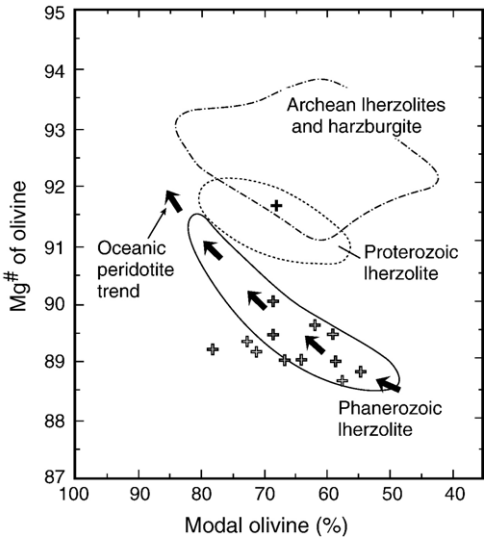

Fig. 9. Olivine Mg# vs. modal abundance for Jünan mantle xenoliths. Oceanic trend is after Boyd [63]; Archean, Proterozoic and Phanerozoic fields are from Griffin et al. [65]. Symbols as same in Fig. 3.

Late Cretaceous (73 Ma) lherzolite xenolith-bearing basalts at Jiaozhou, Shandong Province, which locates to the northeast of Jünan. On the other hand, the occurrence of the high-Mg# peridotite suggests that remnant of the old refractory lithospheric mantle was still preserved beneath the Jiaodong region at least to the eruption of Jünan basaltic rocks. Given the fact that the remnant old lithospheric mantle was also found beneath the Hebi area, Henan Province (the central part of the NCC) [7], the preservation of relics of the old lithospheric mantle beneath the eastern NCC was perhaps a common phenomenon.

Several diverse mechanisms have been proposed to explain the lithospheric thinning processes in eastern NCC. Xu [13] proposed that the thermo-mechanical erosion and chemical erosion played a key role in the destruction of the old lithosphere. In this model, the heating from upwelling asthenosphere weakened the continental base mechanically, and at the same time, melt from low degree partial melting of asthenosphere would infiltrate into and react with the overlying lithospheric mantle, and resulted in upward migration of the lithosphere-asthenosphere boundary eventually. As a consequence, this model will form a lithostratigraphy that the lower parts of the lithospheric mantle are young and fertile in composition, while the upper parts are remnant old lithospheric mantle. Zhang et al. [14], according to the studies of xenocrysts entrapped in the Mesozoic Fangcheng basalts, proposed that crustal melt-peridotite reaction in the mantle was an important mechanism in the transformation of old high-Mg# peridotite to Late Mesozoic low-Mg# peridotites plus pyroxenites, which were considered to be the melting source for the widespread Early Cretaceous calc-alkali volcanic rocks [15]. Yuan [72] and Lu et al. [73] suggested a “Mushroom Cloud” lithospheric structure based on geophysical data since the seismic tomography revealed the existence of both high and low speed anomalies beneath the eastern NCC and the boundaries between these anomalies are precipitous. The hot mantle material corresponding to low speed anomalies is thought to be upwelled from depth greater than 150 km and spread out beneath the crust, and the old lithospheric mantle was enveloped and consumed by the hot, fertile mantle simultaneously. Since the seismic tomographical data have several possibilities that caused the speed anomalies the speed difference may induce from the temperature difference such as induced by melt circulation in the lithosphere rather than the replacement of lithosphere by upwelling asthenosphere.

The equilibrium temperatures of Jünan xenoliths show that there is no obvious difference between the high-Mg# and low-Mg# peridotites, similar to Hebi xenolith locality where the remnant Archean xenoliths occur in the same depth of the phanerozoic xenolith [7]. Though it is difficult to precisely determine the spatial relation between the low-and high-Mg# peridotites due to the scarcity of the high-Mg# samples, the available data suggest that the lithospheric mantle beneath the eastern China is heterogeneous with the co-existence of the newly accreted lithospheric mantle and the old remnant lithospheric mantle. The scarcity of the old remnants represented by the high-Mg# peridotites implies that the majority of the old lithospheric mantle was removed and the newly accreted mantle was dominant in the region.

8. Conclusions

Several conclusions can be reached on the basis of the petrology and mineral compositions of the peridotitic xenoliths entrained in Late Cretaceous Jünan basaltic breecia.

(1) Two types of mantle peridotitic xenoliths exist in the Jünan region, China: the dominant low-Mg# lherzolites (Fo<90), and the subordinate high-Mg# lherzolite (Fo=92).
(2) The low-Mg# lherzolites have petrological and mineralogical affinities to mantle peridotitic xenoliths from the Cenozoic basalts of the NCC,

and thus they represent the newly accreted lithospheric mantle. In contrast, the high-Mg# lherzolite has petrological and elemental features similar to mantle peridotitic xenoliths from Archean/Proterozoic lithospheric mantle and represent the remnant of the old refractory lithospheric mantle.

(3) The thinning of old refractory lithospheric mantle accomplished and the accretion of young fertile lithospheric mantle commenced much earlier than previously thought, i.e. at the Late Cretaceous time.

Acknowledgements

This work was financially supported by Natural Science Foundation of China (40225009; 40534022). Ping Xu and Yuguang Ma are thanked for their assistance in electron microprobe analyses. The manuscript benefits from discussions with Xinhua Zhou. Yanjie Tang and Lianchang Zhang are appreciated for their help in field work and sample preparations. E. Boyle, Yigang Xu and an anonymous reviewer are thanked for their valuable comments which substantially improved the paper.

Appendix A

SIMS analyses of Clinopyroxene standards (ppm)

Element	91CH25-2				91CH48				96CH128				940408B				Average* SIMS / ICP
	ICP-MS	SIMS (n=8)	SIMS/ ICP	Error %	ICP-MS	SIMS (n=9)	SIMS/ ICP	Error %	ICP-MS	SIMS (n=6)	SIMS/ ICP	Error %	ICP-MS	SIMS (n=6)	SIMS/ ICP	Error %	
Sr	23.3	25.6	**1.10**	4	23.1	24.6	**1.06**	9	14.0	16.1	**1.15**	15	9.1	9.0	**0.99**	9	**1.08**
Y	9.0	9.7	**1.08**	5	8.4	8.0	**0.96**	9	33	40	**1.21**	17	1.06	1.18	**1.11**	5	**1.09**
Zr	10.1	10.0	**0.99**	5	7.8	6.6	**0.84**	10	54	70	**1.32**	14	0.18	0.28	**1.54**	22	**1.05**
La	0.71	0.66	**0.92**	5	0.55	0.54	**0.98**	8	1.52	1.39	**0.91**	10	1.22	0.016	**0.01**	10	**0.94**
Ce	2.46	2.60	**1.05**	4	1.79	1.84	**1.03**	8	7.6	7.6	**1.00**	12	0.091	0.074	**0.82**	14	**1.03**
Pr	0.50	0.52	**1.04**	7	0.40	0.35	**0.88**	9	1.81	1.78	**0.98**	12	0.039	0.027	**0.69**	80	**0.97**
Nd	3.05	3.10	**1.02**	6	2.42	2.19	**0.90**	10	11.4	11.7	**1.02**	13	0.177	0.177	**1.00**	65	**0.98**
Sm	1.19	1.24	**1.04**	7	1.07	0.87	**0.81**	9	4.7	4.9	**1.03**	16	0.070	0.084	**1.21**	28	**0.96**
Eu	0.35	0.36	**1.03**	7	0.37	0.33	**0.91**	9	1.04	1.01	**0.97**	12	0.039	0.036	**0.93**	25	**0.97**
Gd	1.68	1.53	**0.91**	17	1.45	1.18	**0.82**	18	6.7	5.3	**0.78**	17	0.155	0.087	**0.56**	73	**0.84**
Tb	0.30	0.26	**0.87**	5	0.25	0.22	**0.88**	13	1.16	1.07	**0.93**	18	0.038	0.027	**0.71**	18	**0.89**
Dy	1.98	1.87	**0.94**	9	1.77	1.55	**0.88**	15	7.7	7.5	**0.97**	15	0.24	0.24	**1.01**	28	**0.93**
Ho	0.41	0.38	**0.92**	7	0.37	0.30	**0.82**	12	1.60	1.54	**0.96**	16	0.047	0.050	**1.07**	21	**0.90**
Er	1.17	1.12	**0.96**	4	1.05	0.90	**0.86**	13	4.5	4.5	**0.99**	19	0.188	0.120	**0.64**	24	**0.94**
Tm	0.166	0.163	**0.98**	14	0.142	0.121	**0.85**	16	0.68	0.61	**0.89**	18	0.019	0.018	**0.95**	27	**0.91**
Yb	1.06	1.10	**1.04**	7	0.91	0.77	**0.85**	12	4.2	4.1	**0.99**	20	0.125	0.137	**1.09**	16	**0.96**
Lu	0.154	0.137	**0.89**	12	0.123	0.112	**0.91**	13	0.63	0.55	**0.87**	19	0.019	0.018	**0.93**	24	**0.89**

*Average SIMS/ICP values for REEs and Zr are obtained without 940408B, which has low REE contents.

References

[1] M.A. Menzies, W.M. Fan, M. Zhang, Palaeozoic and Cenozoic lithoprobes and the loss of >120 km of Archean lithosphere, Sino-Korean craton, China, in: H.M. Prichard, T. Alabaster, N.B.W. Harris, C.R. Neary (Eds.), Magmatic Processes and Plate Tectonics, vol. 76, Geol. Soc. Spec. Pub, 1993, pp. 71–78.

[2] W.L. Griffin, A.D. Zhang, S.Y. O'Reilly, C.G. Ryan, Phanerozoic evolution of the lithosphere beneath the Sino-Korean craton, in: M. Flower, S.L. Chung, C.H. Lo, T.Y. Lee (Eds.), Mantle Dynamics and Plate Interactions in East Asia, Geodynamics Series, vol. 27, American Geophysical Union, Washington, D.C., 1998, pp. 107–126.

[3] J.S. Chi, F.X. Lu, L. Zhao, Kimberlites on the North China Craton and Features of Paleozoic Lithospheric Mantle, Science Press, Beijing, 1996.

[4] J.W. Harris, D.J. Duncan, Z. F., The physical characteristics and syngenetic inclusion geochemistry of diamonds from Pipe 50, Liaoning province, People's Republic of China, in: H.O.A. Meyer, O.H. Leonardos (Eds.), 5th International Kimberlites Conference, Brasilia, 1994, pp. 106–115.

[5] H.O.A. Meyer, A. Zhang, H.J. Milledge, Diamonds and inclusions in diamonds from Chinese kimberlites, in: H.O.A. Meyer, O.H. Leonardos (Eds.), 5th International Kimberlite Conference, Brasilia, Araxa, Brazil, 1994, pp. 98–105.

[6] W. Wang, T. Gasparik, Metasomatic clinopyroxene inclusions in diamonds from the Liaoning province, Geochim. Cosmochim. Acta 65 (2001) 611–620.

[7] J.P. Zheng, S.Y. O'Reilly, W.L. Griffin, F.X. Lu, M. Zhang, N.J. Pearson, Relic refractory mantle beneath the eastern North China block: significance for lithosphere evolution, Lithos 57 (2001) 43–66.

[8] F.R. Boyd, P.H. Nixon, Ultramafic nodules from the Kimberly pipes, South Africa, Geochim. Cosmochim. Acta 42 (1978) 1367–1382.
[9] A.J. Erlank, F.G. Waters, C.J. Hawkesworth, S.E. Haggerty, H.L. Allsopp, R.S. Richard, M.A. Menzies, Evidence for mantle metasomatism in peridotite nodules from the Kimberley Pipes, South Africa, in: M.A. Menzies, C.J. Hawkesworth (Eds.), Mantle Metasomatism, Academic Press, London, 1987, pp. 221–311.
[10] W.L. Griffin, S.Y. O'Reilly, C.G. Ryan, Composition and thermal structure of the lithosphere beneath South Africa, Siberia and China: proton microprobe studies, International Symposium on Cenozoic volcanic Rocks and Deep-Seated Xenoliths of China and its Environs, Beijing, 1992, p. 20.
[11] W.L. Griffin, S.Y. O'Reilly, C.G. Ryan, O. Gaul, D.I. Ionov, Secular variation in the composition of subcontinental lithospheric mantle: geophysical and geodynamic implications, in: J. Braun, J.C. Dooley, B.R. Goleby, R.D. Van der Hilst, C.T. Klootwijk (Eds.), Structure and Evolution of the Australian Continent, Geodynamics Series, vol. 26, American Geophysical Union, Washington D.C., 1998, pp. 1–26.
[12] W.M. Fan, H.F. Zhang, J. Baker, K.E. Jarvis, P.R.D. Mason, M.A. Menzies, On and Off the North China Craton: where is the Archaean Keel? J. Petrology 41 (2000) 933–950.
[13] Y.G. Xu, Thermo-tectonic destruction of the Archaean lithospheric keel beneath the Sino-Korean craton in China: evidence, timing and mechanism, Phys. Chem. Earth (A) 26 (2001) 747–757.
[14] H.F. Zhang, Transformation of lithospheric mantle through peridotite-melt reaction: a case of Sino-Korean craton, Earth Planet. Sci. Lett. 237 (2005) 768–780.
[15] H.-F. Zhang, M. Sun, X.-H. Zhou, W.-M. Fan, M.-G. Zhai, J.-F. Yin, Mesozoic lithosphere destruction beneath the North China Craton: evidence from major-, trace-element and Sr–Nd–Pb isotope studies of Fangcheng basalts, Contrib. Mineral. Petrol. 144 (2002) 241–254.
[16] S. Gao, R.L. Rudnick, H.-L. Yuan, X.-M. Liu, Y.-S. Liu, W.-L. Xu, W.-L. Ling, J. Ayers, X.-C. Wang, Q.-H. Wang, Recycling lower continental crust in the North China craton, Nature 432 (2004) 892–897.
[17] D.Y. Liu, A.P. Nutman, W. Compston, J.S. Wu, Q.H. Shen, Remnants of >=3800 Ma crust in the Chinese part of the Sino-Korean craton, Geology 20 (1992) 339–342.
[18] G.C. Zhao, S.A. Wilde, P.A. Cawood, M. Sun, Archean blocks and their boundaries in the North China Craton: lithological, geochemical, structural and *P–T* path constraints and tectonic evolution, Precambrian. Res. 107 (2001) 45–73.
[19] W.M. Fan, F. Guo, Y.J. Wang, G. Lin, M. Zhang, Post-orogenic bimodal volcanism along the Sulu orogenic belt in Eastern China, Phys. Chem. Earth, Part A Solid Earth Geod. 26 (2001) 733–736.
[20] J.S. Qiu, X.S. Xu, C.H. Lo, Potash-rich volcanic rocks and lamprophyres in western Shandong province: ^{40}Ar–^{39}Ar dating and source tracing, Chin. Sci. Bull. 47 (2002) 91–97.
[21] H.F. Zhang, M. Sun, X.H. Zhou, J.F. Ying, Geochemical constraints on the origin of Mesozoic alkaline intrusive complexes from the North China Craton and tectonic implications, Lithos 81 (2005) 297–317.
[22] J.H. Yang, F.Y. Wu, S.A. Wilde, A review of the geodynamic setting of large-scale late Mesozoic gold mineralization in the North China craton: an association with lithospheric thinning, Ore Geol. Rev. 23 (2003) 125–152.
[23] Y. Xu, X. Huang, J. Ma, Y. Wang, Crust–mantle interaction during the tectono-thermal reactivation of the North China Craton: constraints from SHRIMP zircon U–Pb chronology and geochemistry of Mesozoic plutons from western Shandong, Contrib. Mineral. Petrol. 147 (2004) 750–767.
[24] X.H. Zhou, R.L. Armstrong, Cenozoic volcanic rocks of eastern China-secular and geographic trends in chemistry and strontium isotopic composition, Earth Planet. Sci. Lett. 58 (1982) 301–329.
[25] R.L. Cao, S.H. Zhu, Mantle xenoliths and alkaline rich host rocks in eastern China, in: P.N. Nixon (Ed.), Mantle xenoliths, John Wiley and Sons, Chichester, 1987, pp. 167–180.
[26] B.L. Cong, J.H. Guo, W.J. Liu, A possible relict mantle wedge: geochemical evidence from Paleogene volcanics in North China, Chin. Sci. Bull. 46 (2001) 1917–1922.
[27] A.I. Okay, A.M.C. Sengor, Evidence for continental thrust-related exhumation of the ultra-high-pressure rocks in China, Geology 20 (1992) 411–414.
[28] A. Yin, S.Y. Nie, An indentation model for the North and South China collision and the development of the Tan-Lu and Honam fault systems, eastern Asia, Tectonics 12 (1993) 801–813.
[29] Z.X. Li, Collision between the North and South China blocks: a crustal-detachment model for suturing in the region east of the Tanlu fault, Geology 22 (1994) 739–742.
[30] S.L. Chung, Trace element and isotope characteristics of Cenozoic basalts around theTanlu fault with implication for the eastern plate boundary between North and South China, J. Geol. 107 (1999) 301–312.
[31] R.H. Steiger, E. Jäger, Subcommission of geochronology; convention on the use of decay constants in geochronology and cosmochronology, Earth Planet. Sci. Lett. 36 (1977) 359–362.
[32] M.J. Le Bas, R.W. Le Maitre, A. Streckeisen, B. Zanettin, A chemical classification of volcanic rocks based on the total alkali-silica diagram, J. Petrol. 27 (1986) 745–750.
[33] J.L. Pouchou, F. Pichoir, Quantitative analysis of homogeneous or stratified microvolumes applying the model "PAP", in: K.F.J. Heinrich, D.E. Newbury (Eds.), Electron Probe Quantification, Plenum, New York, 1991, pp. 31–75.
[34] N. Shimizu, M.P. Semet, C.J. Allegre, Geochemical applications of quantitative ion-microprobe analysis, Geochim. Cosmochim. Acta 42 (1978) 1321–1334.
[35] E. Zinner, G. Crozaz, A method for the quantitative measurement of rare-earth elements in the ion microprobe, Int. J. Mass Spectrom. Ion Process. 69 (1986) 17–38.
[36] M. Wiedenbeck, J.M. Hanchar, W.H. Peck, P. Sylvester, J. Valley, M. Whitehouse, A. Kronz, Y. Morishita, L. Nasdala, J. Fiebig, I. Franchi, J.P. Girard, R.C. Greenwood, R. Hinton, N. Kita, P.R.D. Mason, M. Norman, M. Ogasawara, R. Piccoli, D. Rhede, H. Satoh, B. Schulz-Dobrick, O. Skar, M.J. Spicuzza, K. Terada, A. Tindle, S. Togashi, T. Vennemann, Q. Xie, Y.F. Zheng, Further characterization of the 91500 zircon crystal, Geostand. Geoanal. Res. 28 (2004) 9–39.
[37] S. Togashi, N.T. Kita, A. Tomiya, Y. Morishita, N. Imai, Melt contribution to partitioning of trace element between plagioclase and basaltic magma of Fuji volcano, Japan, Appl. Surf. Sci. 203–204 (2003) 814–817.
[38] N.T. Kita, Y. Ikeda, S. Togashi, Y.Z. Liu, Y. Morishita, M.K. Weisberg, Origin of ureilites inferred from a SIMS oxygen isotopic and trace element study of clasts in the Dar al Gani 319 polymict ureilite, Geochim. Cosmochim. Acta 68 (2004) 4213–4235.
[39] N.J.G. Pearce, W.T. Perkins, J.A. Westgate, M.P. Gorton, S.E. Jackson, C.R. Neal, S.P. Chenery, A compilation of new and published major and trace element data for NIS––SRM 610 and

NIST SRM 612 Glass Reference Materials, Geostand. Newsl. 21 (1996) 115–144.
[40] H.G. Wilshire, J.W. Shervais, Al-augite and Cr-diopside ultramafic xenoliths in basaltic rocks from western United States, Phys. Chem. Earth 9 (1975) 257–272.
[41] F.A. Frey, M. Prinz, Ultramafic inclusions from San Carlos, Arizona: petrologic and geochemical data bearing on their petrogenesis, Earth Planet. Sci. Lett. 38 (1978) 129–176.
[42] J.P. Zheng, S.Y. O'Reilley, W.L. Griffin, F.X. Lu, M. Zhang, Nature and evolution of Cenozoic lithospheric mantle beneath Shandong peninsula, Sino-Korean Craton, eastern China, Int. Geol. Rev. 40 (1998) 471–499.
[43] J.P. Zheng, Mesozoic-Cenozoic Mantle Replacement and Lithospheric Thining, East China, China University of Geosciences Press, Wuhan, 1999 (in Chinese with English abstract), 126 pp.
[44] J.L. Bodinier, G. Vasseur, J. Vernieres, C. Dupuy, S.J. Fabri, Mechanisms of mantle metasomatism: geochemical evidence from the Lherz orogenic peridotite, J. Petrol. 31 (1990) 597–628.
[45] E. Anders, N. Grevesse, Abundances of the elements: Meteoritic and solar, Geochim. Cosmochim. Acta 53 (1989) 197–214.
[46] S.S. Sun, W.F. McDonough, Chemical and isotopic systematics of oceanic basalts: implications for mantle composition and processes, in: A.D. Saunders, M.J. Norry (Eds.), Magmatism in the Oceanic Basalts, Special Publication, Geological Society, 1989, pp. 313–345.
[47] P.R.A. Wells, Pyroxene thermometry in simple and complex systems, Contrib. Mineral. Petrol. 62 (1977) 129–139.
[48] T.H. Sachtleben, H.A. Seck, Chemical control of Al-solubility in orthopyroxene and its implicaitons on pyroxene geothermometry, Contrib. Mineral. Petrol. 78 (1981) 157–165.
[49] G. Witt-Eickschen, H.A. Seck, Solubility of Ca and Al in orthopyroxene from spinel peridotite: an improved version of an empirical geothermometer, Contrib. Mineral. Petrol. 106 (1991) 431–439.
[50] G.P. Brey, T. Kohler, Geothermobarometry in four-phase lherzolites II: new thermobarometers, and practical assessment of existing thermobarometers, J. Petrol. 31 (1990) 1353–1378.
[51] R.L. Rudnick, S. Gao, W.L. Ling, Y.S. Liu, W.F. McDonough, Petrology and geochemistry of spinel peridotite xenoliths from Hannuoba and Qixia, North China Craton, Lithos 77 (2004) 609–637.
[52] E. Rampone, P. Bottazzi, L. Ottolini, Complementary Ti and Zr anomalies in orthopyroxene and clinopyroxene from mantle peridotites, Nature 354 (1991) 518–520.
[53] W.F. McDonough, H.G. Stosch, N.G. Ware, Distribution of titanium and the rare earth elements between peridotitic minerals, Contrib. Mineral. Petrol. 110 (1992) 321–328.
[54] E. Hellebrand, J.E. Snow, H.J.B. Dick, A.W. Hofmann, Coupled major and trace elements as indicators of the extent of melting in mid-ocean-ridge peridotites, Nature 410 (2001) 677–681.
[55] O. Navon, E. Stolper, Geochemical Consequences of Melt Percolation- the Upper Mantle as a Chromatographic Column, J. Geol. 95 (1987) 285–307.
[56] Y.-G. Xu, M.A. Menzies, M.F. Thirlwall, X.-L. Huang, Y. Liu, X.-M. Chen, "Reactive" harzburgites from Huinan, NE China: products of the lithosphere-asthenosphere interaction during lithospheric thinning? Geochim. Cosmochim. Acta 67 (2003) 487–505.
[57] J.L. Bodinier, C. Dupuy, J. Dostal, Geochemistry and petrogenesis of eastern Pyrenean peridotites, Geochim. Cosmochim. Acta 52 (1988) 2893–2907.
[58] H.F. Zhang, M. Sun, Geochemistry of Mesozoic basalts and mafic dikes, southeastern North China Craton, and tectonic implications, Int. Geol. Rev. 44 (2002) 370–382.
[59] J. Ying, X. Zhou, H. Zhang, Geochemical and isotopic investigation of the Laiwu-Zibo carbonatites from western Shandong Province, China, and implications for their petrogenesis and enriched mantle source, Lithos 75 (2004) 413–426.
[60] K.T.M. Johnson, H.J.B. Dick, N. Shimizu, Melting in the oceanic upper mantle: an ion microprobe study of diopsides in abyssal peridotites, J. Geophys. Res. 95 (1990) 2661–2678.
[61] M. Norman, Melting and metasomatism in the continental lithosphere: laser ablation ICPMS analysis of minerals in spinel lherzolites from eastern Australia, Contrib. Mineral. Petrol. 130 (1998) 240–255.
[62] Y.G. Xu, M.A. Menzies, J.L. Bodinier, R.M. Bedini, P. Vroon, J.C.C. Mercier, Melt percolation and reaction atop a plume: evidence from the poikiloblastic peridotite xenoliths from Boree (Massif Central France), Contrib. Mineral. Petrol. 132 (1998) 65–84.
[63] F.R. Boyd, Compositional distinction between oceanic and cratonic lithosphere, Earth Planet. Sci. Lett. 96 (1989) 15–26.
[64] D.A. Ionov, I. Ashchepkov, E. Jagoutz, The provenance of fertile off-craton lithospheric mantle: Sr–Nd isotope and chemical composition of garnet and spinel peridotite xenoliths from Vitim, Siberia, Chem. Geol. 217 (2005) 41–75.
[65] W.L. Griffin, S.Y. O'Reilly, C.G. Ryan, The composition and origin of sub-continental lithospheric mantle, in: Y. Fei, C.M. BertKa, B.O. Mysen (Eds.), Mantle petrology: field observations and high-pressure experimentation: a tribute to Francis R. (Joe) Boyd, Special Publicaion, vol. 6, The Geochemical Society, Houston, 1999, pp. 13–45.
[66] P.B. Kelemen, H.J.B. Dick, J.E. Quick, Formation of harzburgite by pervasive melt/rock reaction in the upper mantle, Nature 358 (1992) 635–641.
[67] P.B. Kelemen, S.R. Hart, S. Bernstein, Silica enrichment in the continental upper mantle via melt/rock reaction, Earth Planet. Sci. Lett. 164 (1998) 387–406.
[68] C.T. Herzberg, Formation of cratonic mantle as plume residues and cumulates, in: Y. Fei, C.M. Bertka, B.O. Mysen (Eds.), Mantle Petrology: Field Observations and High-Pressure Experimentation: A Tribute to Francis R. (Joe) Boyd, Special Publication, vol. 6, The Geochemical Socity, Houston, 1999, pp. 241–258.
[69] F.X. Lu, J.P. Zheng, Characteristics of Paleozoic lithosphere and deep processes in the North China platform, in: J.S. Chi, F.X. Lu (Eds.), Characteristics of kimberlites and Paleozoic lithosphere in North China platform, Science Press, Beijing, 1996, pp. 215–274.
[70] H. Zhang, M.A. Menzies, J.J. Gurney, X. Zhou, Cratonic peridotites and silica-rich melts: diopside–enstatite relationships in polymict xenoliths, Kaapvaal, South Africa, Geochim. Cosmochim. Acta 65 (2001) 3365–3377.
[71] J. Yan, J.F. Chen, Z. Xie, Mantle derived xenoliths in the late Cretaceous basalts in eastern Shandong: new constraints on the timing of lithospheric thinning in east China, Chin. Sci. Bull. 48 (2003) 1570–1574.
[72] X.C. Yuan, Velocity structure of the Qinling lithosphere and mushroom cloud model, Sci. Chin (Ser. D) 39 (1996) 233–244.
[73] F.X. Lu, J.P. Zheng, W.P. Li, M.H. Chen, Z.M. Chen, The mantle evolution pattern of Phanerozoic mantle in the eastern China: the "Mushroom Cloud" model, Geosci. Frontier 7 (2000) 97–107.